Title

A flexible adhesive surface electrode array capable of cervical electroneurography during a sequential autonomic stress challenge

Journal

Scientific Reports, 12(1)

ISSN

2045-2322

Authors

Bu, Yifeng

Kurniawan, Jonas F

Prince, Jacob

et al.

Publication Date

2022

DOI

10.1038/s41598-022-21817-w

scientific reports

Check for updates

OPEN

A flexible adhesive surface electrode array capable of cervical electroneurography during a sequential autonomic stress challenge

Yifeng Bu[1,10]✉, Jonas F. Kurniawan[2,10], Jacob Prince[1], Andrew K. L. Nguyen[3], Brandon Ho[1], Nathan L. J. Sit[1], Timothy Pham[4], Vincent M. Wu[5], Boris Tjhia[4], Andrew J. Shin[6], Tsung-Chin Wu[7], Xin M. Tu[7], Ramesh Rao[1], Todd P. Coleman[5] & Imanuel Lerman[1,8,9]

This study introduces a flexible, adhesive-integrated electrode array that was developed to enable non-invasive monitoring of cervical nerve activity. The device uses silver-silver chloride as the electrode material of choice and combines it with an electrode array consisting of a customized biopotential data acquisition unit and integrated graphical user interface (GUI) for visualization of real-time monitoring. Preliminary testing demonstrated this electrode design can achieve a high signal to noise ratio during cervical neural recordings. To demonstrate the capability of the surface electrodes to detect changes in cervical neuronal activity, the cold-pressor test (CPT) and a timed respiratory challenge were employed as stressors to the autonomic nervous system. This sensor system recording, a new technique, was termed Cervical Electroneurography (CEN). By applying a custom spike sorting algorithm to the electrode measurements, neural activity was classified in two ways: (1) pre-to-post CPT, and (2) during a timed respiratory challenge. Unique to this work: (1) rostral to caudal channel position-specific (cephalad to caudal) firing patterns and (2) cross challenge biotype-specific change in average CEN firing, were observed with both CPT and the timed respiratory challenge. Future work is planned to develop an ambulatory CEN recording device that could provide immediate notification of autonomic nervous system activity changes that might indicate autonomic dysregulation in healthy subjects and clinical disease states.

The autonomic nervous system (ANS) links the central nervous system (CNS; brain and spinal cord) with peripheral organ systems, including the integumentary (sweat glands), circulatory (heart, blood vessels), digestive (gastrointestinal tract glands and sphincters, kidney, liver, salivary glands), endocrine (adrenal glands), reproductive (uterus, genitals), respiratory (bronchiole smooth muscles), urinary (sphincters), and visual (pupil dilator and ciliary muscles) systems[1–3]. The ANS is colloquially divided into two main divisions: the sympathetic and parasympathetic nervous systems. However, both branches continuously coordinate through concerted feedback mechanisms to carefully control peripheral organ systems[4,5]. A large body of empirical evidence suggests that autonomic nervous system imbalance is associated with various pathological conditions that can include heterogeneous disease states, such as diabetic autonomic neuropathy, hyperhidrosis, orthostatic intolerance/postural tachycardia syndrome, pure autonomic failure, autonomic dysreflexia, Takotsubo cardiomyopathy, and vasovagal

[1]Department of Electrical and Computer Engineering, University of California San Diego, La Jolla, CA 92093, USA. [2]Materials Science and Engineering Program, University of California San Diego, La Jolla, CA 92093, USA. [3]Department of Physics, University of California San Diego, La Jolla, CA 92093, USA. [4]Department of Nanoengineering, University of California San Diego, La Jolla, CA 92093, USA. [5]Department of Bioengineering, University of California San Diego, La Jolla, CA 92093, USA. [6]Department of Materials Science and Engineering, Stanford University, Stanford, CA 94305, USA. [7]Division of Biostatistics and Bioinformatics, University of California San Diego, La Jolla, CA 92093, USA. [8]Department of Anesthesiology, University of California San Diego, La Jolla, CA 92093, USA. [9]Department of Psychiatry, Center for Stress and Mental Health, VA San Diego, La Jolla, CA 92093, USA. [10]These authors contributed equally: Yifeng Bu and Jonas F. Kurniawan. ✉email: ybu@ucsd.edu

syncope, and it also contributes to pathophysiology associated with autoimmune inflammatory disorders such as Rheumatoid Arthritis[6,7]. Moreover, mental health disorders (e.g., Post-traumatic Stress Disorder (PTSD) and Major Depression Disorder) regularly exhibit circadian autonomic dysregulation, with heightened sympathetic and concomitant low parasympathetic drive most commonly reported[8–12].

The human cervical spine (neck) is the site of a confluence of autonomic neural structures that are in close proximity to each other, including the major parasympathetic neuronal output transmitted by the vagus nerve[13,14]. The vagus nerve communicates directly to the visual, heart, respiratory, and digestive systems, and the major sympathetic neuronal output transmitted by the middle and superior cervical ganglion is located approximately 1–2 cm deep to the vagus nerve[15,16]. The sympathetic ganglion, carotid body, and the vagus nerve are all localized within the carotid artery sheath, and, potentially due to this close proximity, sympathetic fibers have been observed in vagus nerve fascicles (called hitch-hikers), which further indicates multi-sourced neuronal signaling at this cervical level[17]. The superior cervical ganglion and the thoracic sympathetic ganglion output directly to the integumentary, visual, circulatory, respiratory, and digestive organ systems. Given the immense peripheral organ system control generated from cervical autonomic neuronal structures found within the superficial cervical neck[18], decoding these signals to understand the role they play in health and disease could have significant impact on a host of conditions. Prior preclinical work demonstrate resting vagus nerve action potential recording with: (1) cuff electrodes in anesthetized rats during inflammatory cytokine injection[19], (2) carbon nanotube yarn electrodes in anesthetized rats during chronic recording[20], (3) multi-electrode recording cuff electrodes in regularly breathing anesthetized pigs[21], (4) upon stimulation evoked compound action potentials[22], and (5) inserting tungsten microelectrodes into the vagus nerve through ultrasound guidance in awake humans[23]. Further, recent work demonstrate vagus nerve action potentials uniformly synchronize with the respiratory cycle in porcine models[24,25] and in one recent human microelectrode study[23], although synchronized respiratory and cardiac activity may reflect recording modality deployed[26]. Other preclinical work measured (via cuff electrode) superior cervical ganglion activity with hypertensive stress tests, i.e., injection of adrenaline[27,28] or during painful stimuli[29]. These studies uniformly demonstrate immediate (within seconds) change in cervical sympathetic neuronal (superior cervical ganglion) activity with each challenge[27–29]. However, the invasive implantation and the risk and complications associated with acute and chronic surgical cuff electrodes have likely precluded, to date, any reported human cervical vagus nerve, carotid body, or superior cervical ganglion recording with validated stress models.

To enable recording with human autonomic stress models, a noninvasive, adhesive-integrated and skin conformal silver-silver chloride electrode array was developed that is capable of conformal positioning over the human left superior anterior cervical area overlying multiple neural structures (i.e., the vagus nerve and its branches, trigeminal nerve branches, sympathetic chain and its branches, the hypoglossal and glossopharyngeal nerves, as well as muscle and dermal sympathetic nerves), and its ability to monitor cervical nerve activity was tested using two widely used and validated stress tests, the cold pressor stress test (CPT) and a timed respiratory challenge. CPT is performed by immersing the hand into a container filled with ice water, which is known to trigger a sympathetic reaction that involves blood vessel constriction and, thus, an increase in blood pressure[30,31]. It also increases the reflexive modulatory vagal tone by activating multiple brain stem nuclei that coordinate afferent and efferent vagus nerve signaling[32,33]. The effect of CPT—namely pain—on heart rate is bimodal: subjects routinely demonstrated either an increase or a decrease[34,35]. Likewise, in timed respiratory challenge studies, muscle sympathetic nerve activity was bimodal; subjects either increased or decreased muscle sympathetic nerve firing[36]. To date, there is a paucity of inter-challenge analysis within subject physiological measures in response to CPT and timed respiratory challenge. To fill this gap, the newly developed flexible adhesive electrode array was deployed for non-invasive cervical electroneurography (CEN) during a sequential CPT and timed respiratory challenge. Multi-stress challenge CEN measures could help to further disambiguate human autonomic biotypes amongst healthy and disease states in several ways: (1) by facilitating the development of biomarkers of response to pharmacologic and or neuromodulation therapies, (2) enabling the prediction of inflammatory response to pain, and (3) aiding differentiation of sterile vs. non-sterile inflammation.

Results

The custom surface electrode array that was tested is adhesive integrated and flexible, so that it can be non-invasively attached to a subject's anterior cervical neck. The electrode array was placed lateral to the trachea and medial to the sternocleidomastoid for this study. Silver-silver chloride was utilized as the material of choice for the custom electrodes (Fig. 1) in tandem with a customized biopotential data acquisition unit (Fig. 2c). The custom electrode array allowed subjects to freely move (lateral rotation as well as forward, reverse, and lateral flexion and extension) without distorting the adhesiveness and robustness of the physical structure of the electrode array (Fig. 2a,b)[37]. The impedance between the custom surface electrode array and the skin was maintained at 1.6 kΩ or less over a 2-h period of testing time; whereas consistent impedance maintenance over a 2-h period is considered ideal for electrical physiological recording[38]. With consistent low impedance we observed a concordant decrease in power line noise and its harmonics[39,40].

Cervical electroneurography recordings were carried out with four electrode "channels" positioned rostral to caudal to evaluate cervical signal: (1) pre-to-post CPT and (2) during a timed respiratory challenge. All channels were run through a spike sorting algorithm to identify putative action potentials or nerve firing patterns associated with different nerve branches. Instantaneous heart rate (beats per minute) at each heartbeat was derived by dividing the 60 (s/min) by the extracted RR intervals calculated from our ECG recordings.

In a sample subject, the change in cervical neural firing was observed to coordinately increase with onset of CPT; the cervical neural firing was extrapolated from the spike sorting algorithm (Fig. 3a). Simultaneous recordings from Channel #1 (rostral overlying nodose ganglion, C2/3 cervical dermatome, and auriculotemporal

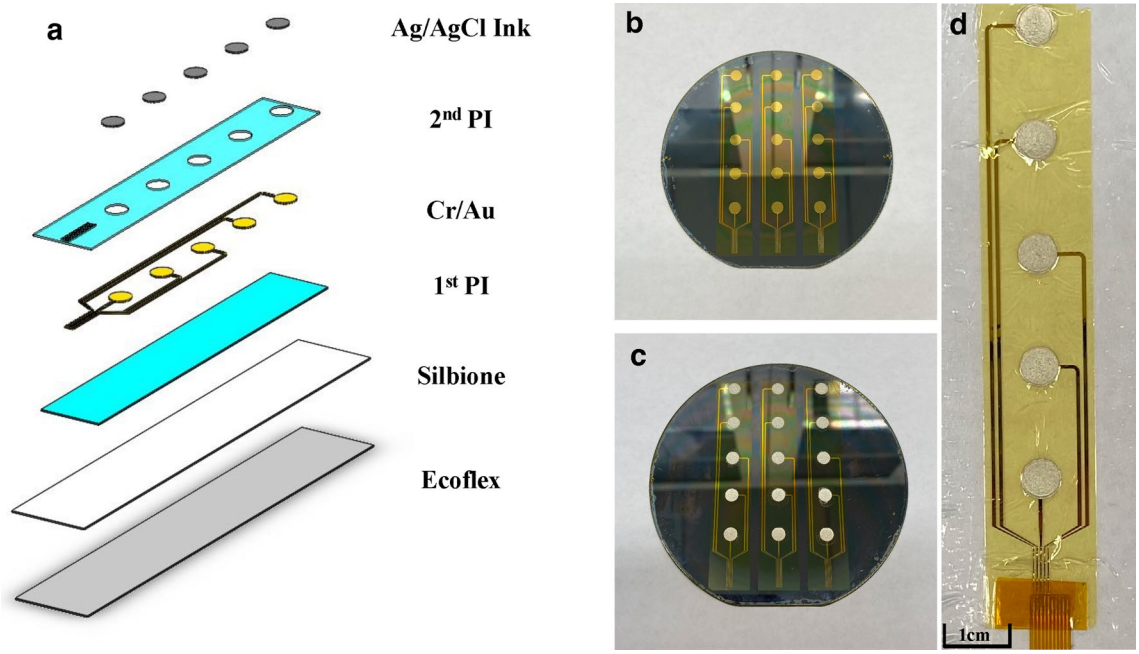

Figure 1. Custom surface electrode array for non-invasive testing of cervical neuronal activity. (**a**) Device cross section (5 mm sensor diameter and 500 µm interconnect width). (**b**) Cleanroom post-processed wafer ready to be printed with Ag/AgCl ink. (**c**) Ag/AgCl ink screen-printed wafer on the active electrode region. (**d**) Device transfer-printed onto a self-adhering flexible silicone substrate (Ecoflex/Silbione) on PET backing via water soluble tape.

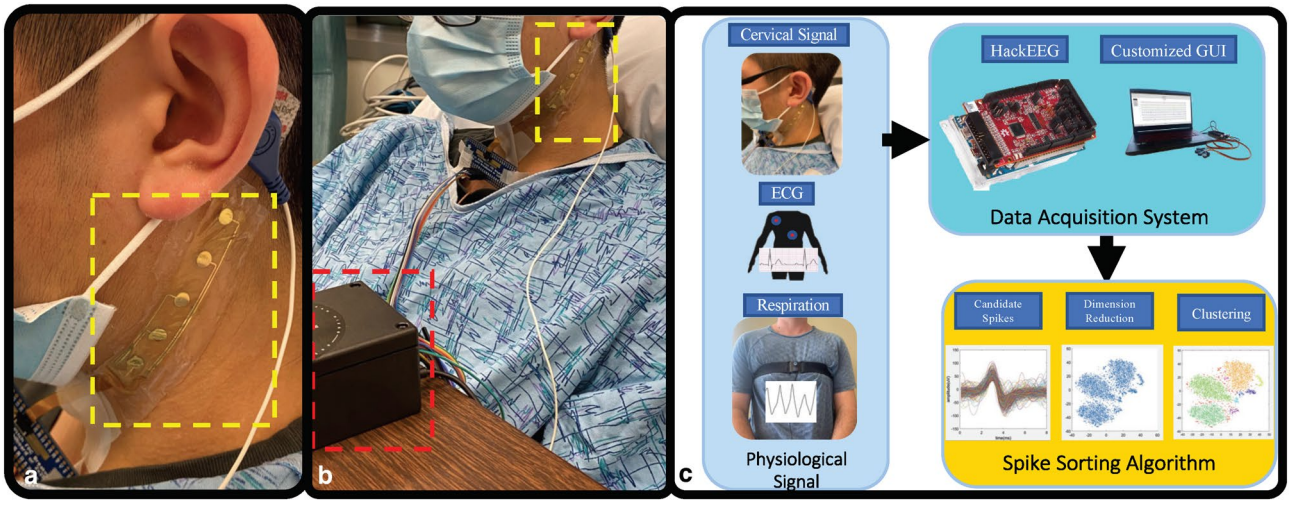

Figure 2. The custom design allows for free movement without distorting the adhesiveness and robustness of the physical structure of the electrode array. (**a**) The custom surface electrode array is adhesive integrated, flexible, and non-invasively attached to the subject's anterior cervical neck, placed lateral to the trachea and medial to the sternocleidomastoid. A 3 M RedDot electrode was used as a reference electrode. The four channels were aligned rostral to caudal, so that each channel was positioned over an anatomical target: (1) channel #1 over the upper nodose ganglion, (2) channel #2 over the lower nodose ganglion, (3) Channel #3 over the upper carotid artery, and (4) channel #4 over the lower carotid artery. (**b**) Data collection was carried out with flexible multi-electrodes attached to the wireless biopotential data acquisition board, i.e., the HackEEG (red dashed outline), and 3 M RedDot deployed as ground/reference electrodes. (**c**) Subject recording pipeline and workflow. Cervical electroneurography, electrocardiography, and respiration were recorded; signals recorded to the data acquisition system underwent post processing algorithms.

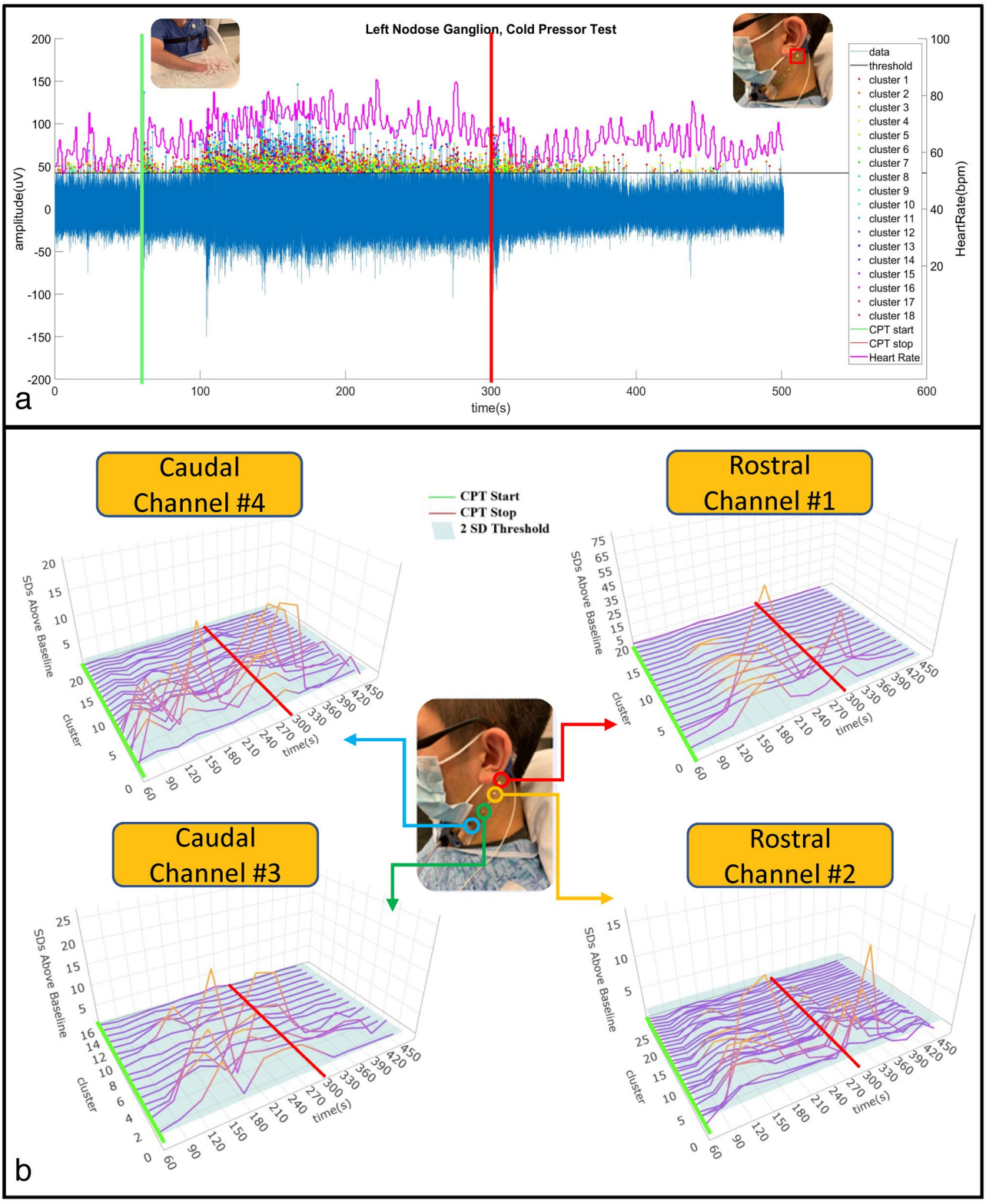

branch of the trigeminal nerve) and heart rate were compiled (Fig. 3a). Amongst an array of clusters, responsive clusters were identified. Responsive clusters were defined as clustered groups that significantly increased in firing (by greater than 2 standard deviations) during CPT (for at least 40% of the stress challenge) compared to pre-CPT baseline activity.

With the CPT challenge, approximately 20 unique spike clusters were recorded in each subject. Spike cluster firing activity was evenly divided into 5 temporally separated intervals over the duration of the CPT (0–20%, 20–40%, 40–60%, 60–80%, and 80–100%) with the aim of meticulously measuring onset and decline of neural

◂**Figure 3.** Cervical neural firing coordinately increases with onset of CPT. (**a**) Cervical Electroneurography (CEN) rostral Channel #1 recording post-spike sorting analysis for the cold-pressor test (CPT). The green vertical line indicates CPT start i.e., the subject immersed their right hand into the ice-water bucket, while the red vertical line indicates CPT cessation i.e., the subjects removed their hand from the ice water bucket. Channel #1 (blue line = neural firing) captures the amplitude of the recorded neural action potential data. The peak of each detected spike (blue line) that exceeds the threshold value sorted each to 18 different clusters identified by different color. Heart rate in beats per minute is plotted in magenta using the right y-axis. (**b**) Exemplar subject cervical electroneurography (CEN) neural firing change during the cold pressor test. *Top left* Responsive clusters at the Caudal Channel #4 (located over the carotid artery, vagus nerve, glossopharyngeal nerve, sympathetic chain, and sensory C2/C3 dermatomal nerves) immediately increase in firing frequency with cold pressor test (CPT) onset (i.e., hand placed in ice water bath). *Top right* Responsive clusters from the rostral Channel #1 (located over nodose ganglion and in close approximation to the auriculotemporal nerve) demonstrate delayed firing onset (at 120–150 s). *Bottom panels* Both Caudal Channel #3 (overlying the carotid artery, vagus nerve, glossopharyngeal nerve, sympathetic chain, and sensory C2/C3 dermatomal nerves) and Rostral Channel #2 (located over nodose ganglion and in close approximation to the auriculotemporal nerve) increase in firing frequency at 90–120 s post recording initiation. In all panels, the transition from purple to orange lines indicates increases in cervical neural firing greater than 2 SD above baseline (i.e., prior to CPT start), and the green line denotes initiation of CPT, while cessation is denoted by the red line.

firing. Percent duration was employed to allow for temporal normalization of measures during the CPT. Average firing change (normalized by baseline activity) for each channel across all clusters was computed at each CPT time interval and compared as follows: (1) within channel to baseline firing and (2) between channels at each time interval (Fig. 4). Because individual pain experience mediates effects of noxious stimulus and the psychological factor such as expectation can shape reflexive responses, there are large distributions of the neuronal firing ratio change during CPT[41,42]. We found that all four channels at both the 0–20% and the 20–40% intervals showed significant increased firing activity when compared to baseline ($p < 0.05$). During the 0–20% CPT interval, Channel #4 (lower carotid artery) demonstrated greater neural firing ($p < 0.05$) when compared to both Channel #1 (over nodose ganglion) and Channel 2 (over lower nodose ganglion and 3rd trigeminal nerve, i.e., the auriculotemporal branch) as shown in Fig. 4. Furthermore, during the 20–100% intervals of CPT, the increase in overall firing was observed to be greater for Channel #2 than for Channel #4 (Fig. 4b–d).

Prior work by Mourot et al.[35] categorized subjects into two separate biotype groups, Cold Pressor Test Increaser (CPTi) or Cold Pressor Test Decreaser (CPTd), based on their heart rate (HR) responses under CPT (see methods). In this CPT experiment, similar group/biotypes to those described by Mourot and colleagues[35] were observed that were also equally distributed between CPTd ($N = 5$) and CPTi ($N = 4$). Building on Mourot's biotype categorization (i.e., groups separated based on CPTd or CPTi), we aimed to determine if nested biotypes could be observed during the CPT as well as during the timed respiratory challenge. During the CPT, greater neural firing ($p < 0.05$) was observed in the CPTi compared to the CPTd group for the first two intervals (0–20% and 20–40%) and across all channels (Supplemental Fig. 1). The spline generalized estimating equations (GEE) showed that the change in firing frequency from 0 to 50 s was different between two CPT groups at Rostral Channel #2, Caudal Channel #3, and Caudal Channel #4 at the trend level ($p < 0.1$) (Supplemental Table 1, Supplemental Fig. 2). The models also show that the slope change in firing frequency from 0–50 s to 50–200 s was met a trend level in between CPT groups across all four channels ($p < 0.08$) (Supplemental Table 1). Moreover, biotype-specific (CPTd vs. CPTi) changes in average CEN firing were observed over the duration of the timed respiratory challenge. Specifically, neural firing during pre-respiratory (initial 60 s) challenge was compared to neural activity during post-respiratory challenge (post 60 s) between groups (CPTd vs. CPTi). Significant increases in CEN firing were observed across all 4 channels during the timed respiratory challenge, while the inverse was observed in the CPTd group, which showed decreases in CEN firing over the timed respiratory challenge with significant changes noted in Channel #4 (Fig. 5). Differences in CEN change pre-to-post timed respiratory challenge were identified between groups (CPTd vs. CPTi) across all channels, with the greatest change noted in Channel #1 (Fig. 5c). GEE analysis showed significant group effect on pre-to-post respiration neural firing change across all channels ($p < 0.02$; Supplemental Table 2). Moreover, in addition to the observed group effect on neural firing (both during CPT and timed respiratory challenge), there was a significant effect (CPTd vs. CPTi) on heart rate during the timed respiratory challenge (Supplemental Fig. 1a).

Discussion

Electrode array fabrication and data collection. In this study, a flexible, adhesive-integrated electrode array was presented for the non-invasive monitoring of neural activity at the anterior cervical area. This approach was inspired from a well-studied and understood flexible electronics platform that was first pioneered in 2011[43]. Manifest in our study is a hybrid approach that combines thin film microfabrication technology with thick film screen printing technology, as has been recently demonstrated by our group[44,45]. Without further testing of its mechanical properties during this study, the electrode array was designed following mechanical guiding principles of flexible electronics that were shown in a prior study[37]. As in our prior work, the sensor layer was placed in between polyimide layers which will place it in a neutral mechanical plane (undergoing very little tension or compression during bending); it therefore enables mechanical robustness of the sensor array.

The peel-and-stick device replaced the use of an invasive and cumbersome needle electrode. Because of the self-adhering and non-invasive design of the electrode array, the array enabled the measurement of electrical signals over a prolonged period[44]. In terms of structural benefit, the flexible sensory array enabled conformal

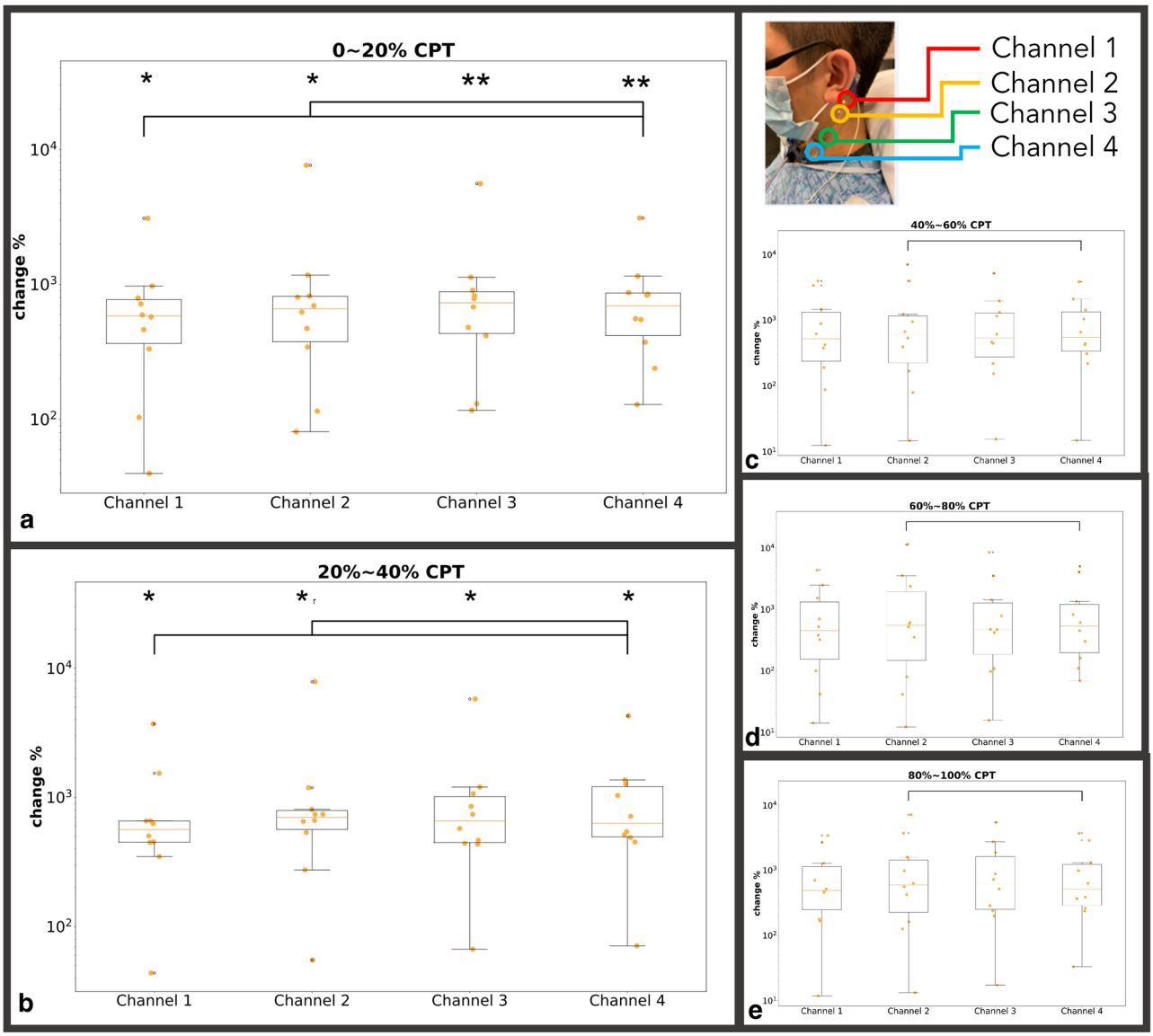

Figure 4. All subject channel activity across CPT indicated as % time intervals: (**a**) 0–20% of CPT; (**b**) 20–40% of CPT; (**c**) 40–60% of CPT; (**d**) 60–80% of CPT, and (**e**) 80–100% of CPT duration. Panel A: For the first interval of 0–20%, Channels #3 and #4 demonstrate highly significant increases in firing frequency (**$p < 0.001$), while Channels #1 and #2 also increased in firing frequency, but to a lesser extent (*$p < 0.05$) when compared to baseline. Channel #4 (lower carotid artery) demonstrated significantly greater (connected segment) firing than Channels #1 and #2 ($p < 0.05$). Panel (**b**) All channels remained at relatively increased activity ($p < 0.05$) when compared to baseline. An increase in firing in Channel #2 was observed when compared to Channel #4 ($p < 0.05$). Panels (**c**–**e**) All channels do not show increases in activity when compared to baseline. Channel 2 continued to demonstrate significantly greater firing than Channel 4 for the remaining CPT duration ($p < 0.05$). Channel #1 = overlying upper nodose ganglion; Channel #2 = overlying lower nodose ganglion and trigeminal auriculotemporal branch; Channel #3 = overlying upper carotid artery; Channel #4 = overlying lower carotid artery. X Axis: Channel 1–4; Y Axis: Percentage Increase in neural firing frequency with respect to baseline activity.

contact with the human skin which will further reduce noise during recording. The usage of Ag/AgCl, the material of choice when performing electrophysiology measurements, was recently shown to reduce recording noise in this hybrid screen-printed format[44]. Further, the fabrication process of these sensor array is compatible with standard microfabrication procedures that are easily replicated in a university/industrial cleanroom setting[43–45].

For the electrode design, Ag/AgCl was chosen as the sensor layer material due to high signal-to-noise ratio, lower skin-to-electrode impedance, and the non-polarizable nature of Ag/AgCl electrodes, which allows the Cl^- ion to take part in free charge exchange, preventing charge buildup[45–48]. Thin film technology enabled a high-resolution interconnect array that allows us to keep the form factor of the connector cable with 0.50 mm width (standard width used for a zero-insertion force (ZIF) connector interface). The sensors were built using standard microfabrication processes followed by screen printing of Ag/AgCl ink, which yielded a final product

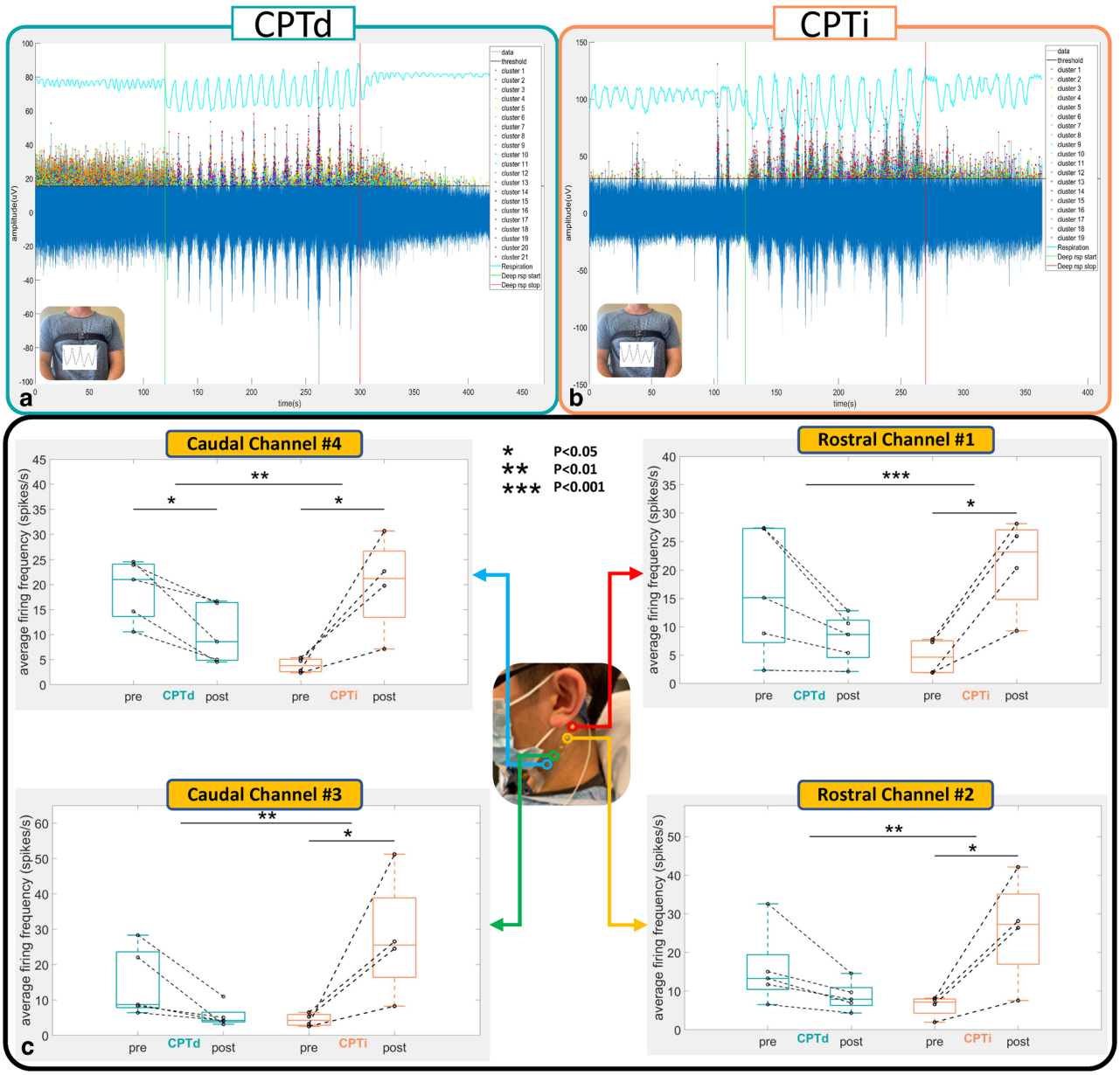

Figure 5. Neuronal firing comparison between CPTd and CPTi groups during the respiratory challenge. (**a**, **b**) The green vertical line indicates initiation of the respiratory challenge, while the red vertical line indicates cessation of the respiratory challenge. The blue line captures the amplitude of the recorded electrode data for electrode positioned over the upper nodose ganglion (Channel #1). The peak of each detected spike (exceeding the threshold value) is indicated by spike coloraction in the positive y-axis, representing the different clusters. The respiration belt voltage is plotted in cyan using the right y-axis. (**a**) Exemplar CPTd CEN neural firing change during deep respiratory challenge. (**b**) Exemplar CPTi CEN neural firing change during deep respiratory challenge. (**c**) Average firing frequencies comparison between pre- and post-challenges for CPTd and CPTi groups across four channels. All channels in the CPTi group have significant neuronal activity increase after deep respiratory challenge ($p < 0.05$), whereas only Channel #4 in the CPTd group has significant decreased activity. We observed significant between group (CPTd vs CPTi) differences ($p < 0.01$) in neuronal firing change across all channels.

that combined the best properties of each fabrication method (thin film and thick film). The thick-film technology enabled delivery of micrometer-thick Ag/AgCl ink that otherwise would not have been possible to deposit in a thin film process. Previously, it was demonstrated that flexible electrodes utilizing Ag/AgCl (developed by our group) were successful in measuring other biopotential signals, such as electrogastrogram (EGG)[45]. Taken together, the developed Ag/AgCl electrode enabled a high-fidelity, low noise recording for this study's application.

In terms of the application of the electrode during recording sessions, overlying the electrode array at the left superior anterior cervical area spanning rostral to caudal in a diagonal fashion enabled measurement of

biopotentials from the skin surface that could arise from the activation of multiple superficial and deep neural structures during CPT and a timed respiratory challenge. The nerve structures that could be measured by the electrode array include the vagus nerve and its branches, the sympathetic chain of interconnected ganglia, the hypoglossal nerve, and glossopharyngeal nerves, as well as muscle electric signals and the potential activity of dermal sympathetic nerves. These neural recordings provided a sufficient signal-to-noise ratio to enable an electrocardiographic-derived heart rate estimate and neuronal spike sorting throughout the CPT. Moreover, spike sorting of signals collected from the different channels of the electrode array revealed statistically significant temporal and spatial relationships. One basic requirement for spike sorting is the spatial relationship between channels. In the presented electrode device, both the electrode size and associated impedance, as well as the electrode shape and its arrangement on specific patterns can be customized[44]. Electrochemical impedance characterization of the 5 mm electrode diameter (5 mm utilized in this current study) has been fully characterized by our groups prior work[44,45]. With this in mind, the versatility of electrode shaping can aid in neural structure source identification. Accurate CEN potential sourcing of underlying neural structures may provide a powerful tool to evaluate sympathetic versus parasympathetic activity and their correlated homeostatic processes. Once these signal-sourcing challenges can be resolved, CEN may prove a valuable tool for assessing body homeostasis.

The processing pipeline and electrode design were constructed to enable convenient and accurate neuronal recording. Specifically, an open-source HackEEG data acquisition unit was integrated with a Texas Instruments ADS1299 chip, which can sample 8 channels of data at a 16 k sampling rate with 24-bit ADC resolution. Because the neural activity targeted in this study is less than 1000 Hz[49], an 8000 Hz sampling rate was implemented, which efficiently enabled accurate reconstruction of critical spike neuronal waveforms. During measurements, the customized GUI was able to plot recordings in real time to monitor responses and abnormalities. Together, monitoring via the HackEEG biopotential board and the custom GUI with our electrode array allowed for convenient recording of the subjects' CEN. A future next step is to interface the flexible electrode array with the necessary remaining hardware to amplify, digitize, and wirelessly broadcast the neural signals recorded, thus allowing ambulatory use.

CPT neuronal response. The electrode design, recording technique, and electrode placement enabled the measurement of multiple neuronal signals characteristic of different possible sources. As in prior work, dermal sympathetic nerve firing, also referred to as skin sympathetic nerve activity, was ultimately detected, which is known to immediately increase with CPT onset; specifically, dermal sympathetic sudomotor firing results in eccrine sweat gland excretion that increases skin conductance, a phenomenon also known as electrodermal activity (EDA)[49,50]. Other sources of signals likely were detected as well, including deeper muscular sympathetic neurons, carotid bodies, sympathetic chain, and ganglia spanning the carotid body, middle and superior cervical ganglion, in addition to action potentials emanating from the glossopharyngeal nerve, the vagus nerve and its rostral ganglia, the nodose and jugular ganglia.

Spike sorting the electrode array CPT recordings enabled identification of key temporal and spatial signal characteristics that could reflect different neural source responsivity to the CPT. As part of the spike sorting analysis, the detected spike waveforms were decomposed from each measurement into multiple clusters. After applying spike sorting to the measured signal, it was found that amongst all channels (Rostral to caudal Channel #1 = overlying upper nodose ganglion, Channel #2 = overlying lower nodose ganglion, Channel #3 = overlying upper carotid artery, Channel #4 = overlying lower carotid artery), multiple neural clusters had significant increases in firing compared with baseline during CPT, followed by a gradual return to baseline upon CPT termination (Fig. 3b). Specifically, the neuronal firing was most significant ($p < 0.05$) during the first two (0–20% and 0–40% periods) of the five CPT time intervals (Fig. 4). Importantly, this array detected temporal distributed neuronal activity; we demonstrate that the presented pipeline could detect (within 1 min) increases in cervical neuronal activity known to occur with CPT[30–34]. Additionally, this activity pattern followed the expected effects of CPT on several neuronal structures within the coverage of the anterior CEN array, including the vagus nerve (increased vagal tone during CPT)[31,32], muscle and skin sympathetic nerve activity or EDA (increased activity followed by return to baseline), and carotid bodies (responsive to CPT induced increases in blood pressure)[33,49]. Collectively, the presented electrode array enabled the non-invasive detection and cluster isolation of neuronal spikes corresponding to CPT that may emanate from an aggregation or component of the vagus nerve, dermal skin, muscle, and carotid body sympathetic response, while other neural structures may also contribute.

Unique to this study, significant spatiotemporally distinct cluster responsivity was observed when comparing Channels #1 and #2 (overlying the rostral auriculotemporal nerve and nodose ganglion) to Channels #3 and #4 (overlying the caudal carotid artery and sympathetic chain ganglia). Specifically, during the first 0–20% interval of the CPT, the caudal carotid artery sensor (Channel #4) demonstrated significantly higher firing frequency than the rostral nodose ganglion sensors (Channels #1 and #2) ($p < 0.05$) (Fig. 4). In contrast, during the 20–100% intervals of the CPT, the rostral nodose ganglion sensor (Channel #2) showed significantly higher firing frequency when compared to that of the caudal carotid artery sensor (Channel #4). Moreover, both caudal carotid artery sensors (Channels #3 and #4) demonstrated highly significant ($p < 0.001$) increases in firing frequency during the first interval of 0–20%, while the rostral sensors (Channels #1 and #2) also captured increased firing, but to a lesser degree than the caudal sensors (Channels #3 and #4) ($p < 0.05$) (Fig. 4).

Prior work provided a premise for the observed delayed activity at the rostral Channels #1 and #2 (positioned over the trigeminal auriculotemporal branch distribution) when compared to the caudal Channels #3 and #4 (positioned over the carotid artery, carotid body, and sympathetic chain). In experimental studies of motion sickness[51–53] and virtual reality (VR) experiments that looked at "cybersickness"[52], immediate extremity dermal sympathetic neural activity was regularly observed; *however, increases in forehead (Trigeminal Nerve distribution) dermal sympathetic neural activity were delayed by several minutes or until coinciding nausea symptomatology*

began[51–53]. Vagus afferent and efferent signaling are well established as key mediators of nausea and vomiting[54–56]. Additionally, previous studies have shown coordinated decreases in vagus mediated high frequency heart rate variability (HRV) with the onset of nausea symptomatology in motion sickness, whereas the onset of strong nausea was proceeded by bursting increases in high frequency HRV[57–59]. Likewise, vagus mediated high frequency HRV measures highly correlate with motion sickness/cybersickness onset with VR gameplay[60]. High frequency HRV is often used as a proxy for vagus nerve activity and its effects on parasympathetic output[61–63] and is supported by cuff electrode vagus nerve firing correlates of HF HRV, while the reciprocal, i.e., inverse/negative correlation of vagus cuff firing to LF HRV, has not been reported to date[64]. Furthermore, electrogastrography (EGG) measures slow wave myoelectric activity in the stomach that is modulated by vagus nerve signaling[65] and decreases with motion sickness/cybersickness onset[66,67]. Our group showed that gastric antrum stimulation decreases EGG slow wave power[16], which is consistent with recent pre-clinical work by Tan et al.[68]. Moreover, our group showed brainstem, lower medulla, dorsal motor nucleus of the vagus (DMX), nucleus tractus solitarius (NTS), and rostral ventrolateral medulla (RVLM) blood-oxygen-level dependent (BOLD) activation with thermal pain[69]. Recently, others have now confirmed these specific brainstem activation patterns in numerous experimental pain paradigms, such as mechanical[33,70], thermal[69], and CPT[33]. Remarkably, these brainstem areas that coordinate complex autonomic neural circuitry, including vagal parasympathetic (DMX, NTS) and sympathetic nuclei (RVLM), demonstrated a relative delay in onset activation (similar to delays observed with motion and cybersickness) when compared to cortical clusters, including the supplementary motor and insular cortices[70]. Collectively, these studies indicate that delayed changes in vagus nerve signaling, as well as specific dermatomal sympathetic neural activity "reflex circuits," coordinate in tandem with onset of nausea in motion/cybersickness and during experimental pain paradigms such as CPT. In this study, these constructs are supported by the observation that caudal Channels #3 and #4 (positioned over the carotid artery, carotid body, and sympathetic chain) immediately (0–20% CPT interval) increased in neural sympathetic activation, while Channels #1 and #2 (positioned over the trigeminal auriculotemporal branch distribution) showed relatively less activity at this interval. However, greater activity in Channel #2 compared to Channel #4 was observed during 20%-100% CPT interval. As sympathetic output to the forehead is controlled by the Trigeminal nerve, the relative delay in neural firing in Channels #1 and #2 (positioned over the auriculotemporal branch of the Trigeminal nerve and the nodose ganglion) coincides with previous reports that demonstrate a delayed increase in trigeminal nerve sympathetic output that is known to occur with vagal-mediated reflex stress responses, associated with onset of motion/cybersickness, and CPT[51–53]. Future work will measure EGG, magnetoencephalography (MEG), and cervical electroneurography (CEN) during CPT to record multi-sourced coordinate neural changes that may further identify high resolution temporally dependent autonomic reflexes and give insight into visceral-brain coupling recently observed between EGG and MEG recordings[71].

CPTd and CPTi biotypes. Distinctive to this study, subjects underwent two sequential autonomic stress tests (i.e., the timed respiratory challenge followed by the cold pressor test) while simultaneously recording heart rate and CEN change in neural firing. Human defense responses covary with autonomic regulatory response subtypes; individuals regularly demonstrate distinct autonomic biotypes with noxious stress challenge tests such as cold pressor (i.e., CPTd and CPTi)[31,72–78]. In this study's cohort, an approximately equal number of subjects were categorized as CPTd (N = 5) and CPTi (N = 4). Extraordinarily, biotype-specific change in average CEN firing during the CPT and timed respiratory challenges was consistently observed (Fig. 5, Supplement Figs. 1, 2). To our knowledge, this is the first cross challenge report that indicates a direct relation between timed respiratory challenge CEN and heart rate change during CPT. Prior work by our group demonstrated that pre-deployed warfighter dysautonomia is predictive of eventual development of post-traumatic stress disorder (PTSD) in servicemembers[79]. Because PTSD is known to have a baseline hyper-sympathetic drive, it is concordantly comorbid with cardiac disease risk[80]. Therefore, it was postulated that the hyper-sympathetic timed respiratory challenge response identified in the CPTi group may indicate a biotype at risk for mental health disorder and or hyperinflammatory response. In support of this construct, PTSD sympathetic neural firing is highly increased during CPT when compared to healthy controls[81]. While our group observed hyper inflammation and hyper-sympathetic drive in PTSD individuals whom undergo intravenous Lipopolysaccharide injection[82,83]. Future work will determine if CEN-derived hyper-sympathetic biotypes can predict immune cell response in additional in-vivo human inflammatory model (intravenous lipopolysaccharide injection) in both healthy and PTSD patients and in hospitalized pre-septic patients.

Limitations. Although these findings are promising, the present study has several limitations. First, the data are cross-sectional with relatively small sample size. This pilot study was meant to demonstrate feasibility of the flexible, adhesive-integrated electrode array for CEN recording during validated stress challenges, i.e., CPT and timed respiratory challenge. These findings need to be validated in a larger study cohort of healthy subjects and patients with a mental health disorder, namely PTSD. In addition, these findings would have more impact if the study were done in larger populations of both sexes, with the aim to identify sex-specific effects. For instance, we did not control for menstrual cycle for all female participants, which could impact CEN recording during CPT[81]. Prior work also demonstrated that sympathetic responses are both longer in duration and larger in amplitude during afternoon testing[84]. Although we did not control for exact time of day for the timed respiratory challenge or CPT, all testing occurred within the window of 13:00 to 18:00 and not during nighttime hours.

Upon subject hand insertion into the ice water bucket unavoidable small movement (adjustments) can occur due to noxious pain; thus these small movements may potentially cause sternocleidomastoid muscle (SCM) electromyography (EMG) artifacts. We identified transient large amplitude neural firing indeed suspected to be EMG artifact differentiable when compared to smaller amplitude continuous neuronal activity recorded; during CPT

we identified likely SCM EMG activity occurrence at a rate of 1.52 ± 2.37% amongst the total CPT time across all 10 subjects. No significant difference was found between CPTd and CPTi group in terms of the SCM activity ratio during CPT and SCM activity firing rate (Supplementary Fig. 3). EMG activity remained in our analysis as to more accurately reflect the whole person response. Although not significantly different in this analysis, we suspect (as prior demonstrated[31,35,42,72–78,85]) differences in the noxious painful experience may contribute to small movements observed and may reach significance in a larger cohort. In prior literature, experimental deep breathing coincides with SCM large amplitude EMG activity[86,87]. In our cohort we also measured deep breathing-coupled EMG activity. In our analyses we excluded recording during the deep respiratory challenge (inclusive of this respiratory SCM large amplitude EMG artifact) as we are specifically interested in the dynamic/temporal autonomic change pre and post the deep breathing challenge. Prior work demonstrate respiration cycle duration (i.e., the period) is linearly related to the depth of each breath[88]. Inter-individual breathing depth change pre-to-post the deep breathing challenge was not different amongst all subjects ($p = 0.1225$, Supplementary Fig. 3). When comparing CPTd and CPTi (pre-to-post deep breathing challenge) no difference in breath cycle was observed ($P = 0.6427$); therefore, we postulate no difference in breath depth between groups.

Conclusion

We observed three notable findings: First, a flexible, adhesive-integrated electrode array was shown to be capable of non-invasive monitoring of cervical neuronal activity (spike cluster firing) during two validated stress challenges, CPT and timed respiratory challenge. Second, significant spatiotemporally distinct sensor-specific cluster responsivity was observed; rostral channels (overly trigeminal and vagus nerve branches) demonstrated less activity during the first portions of the CPT with a rebound increase during the last half of the CPT, emulating the neural activity observed in motion and cybersickness. Third, a consistent composite biomarker incorporating CEN and HR change was identified across both the CPT and the timed respiratory challenge, it may indicate and or predict a conserved autonomic biotype. In aggregate,we developed a flexible adhesive electrode array that is capable of non-invasive detection of ANS change in activity (via CEN and ECG) across multiple validated stress challenges. More work is required to confirm CEN robustness and capability to derive biotypes in healthy control and patient populations.

Methods

Electrodes array fabrication. A 4″ silicon wafer was cleaned with acetone, isopropyl alcohol (IPA), deionized (DI) water, and IPA again followed by drying with an N_2 gun. The wafer then underwent a dehydration bake at 180 °C on a contact hotplate. Subsequently, polydimethylsiloxane (PDMS), which acts as a weakly adhering substrate, was spun coated at 4000 rpm. Polyimide (HD Microsystems, Inc.—Parlin, NJ) was then spun coated at 4000 rpm followed by a soft bake at 110 °C for 1 min and at 150 °C for 5 min on a contact hotplate. A full hard bake in an N_2-rich environment oven at 300 °C then followed. Metallization was performed on an electron beam evaporator (Temescal BJD 1800 E-Beam Evaporator—Livermore, CA) to yield a 10 nm chrome and a 500 nm gold layer. Sensors (5 mm diameter) and interconnects (500 µm width) were then defined via standard lithographic procedures. Another layer of polyimide was then applied using the same parameters as above. Photolithography and reactive ion etching (RIE) with O_2 plasma followed to define the bottom and top polyimide layers, which acted as insulator layers.

Post cleanroom processing, a silver/silver chloride ink (Creative Materials, Inc.—Ayer, MA) was screen printed onto the active sensor areas via a standard stainless-steel stencil (Metal Etch Services, Inc.—San Marcos, CA). A custom zero insertion force (ZIF) connector was then interfaced with the electrode array using anisotropic tape (3 M, Inc.—Saint Paul, MN) to facilitate bonding by applying heat and pressure on the bonding sites. Water soluble tape (3 M, Inc.—Saint Paul, MN) was then used to transfer print the device from the silicon wafer to a flexible silicone substrate made on a 5″ petri dish that was spun coated at 3000 rpm with Ecoflex (Smooth On, Inc.—Macungie, PA), which acted as a backbone silicone, and Silbione RT Gel (Elkem, Inc.—Brunswick, NJ), which acted as an adhesive silicone. The silicone substrate and the device were then peeled off and transferred to a thin sheet of polyethelene terephthalate (PET) (Grafix—Maple Heights, OH), which acted as a backing that eased handling of the device. The silicone bilayer was then cut into a rectangular shape, which yielded the final sensor array as shown in Fig. 1.

Participants. A total of 10 mentally and physically healthy subjects (2 females and 8 males, ages 21.8 ± 2.1) were recruited and enrolled in the study. The study was approved by the University of California San Diego Institutional Review Board (IRB#171154) and all research was performed in accordance with guidelines and regulations. All subjects provided written informed consent prior to participation and agreed to disclose identifying images for open-access publication.

Electrode placement. EC3 Conductive adhesive gel (Natus Medical Incorporated. CA, USA) was applied to the electrode surface using a syringe to improve conductivity. The device was then applied to the neck with the rostral electrode approximately at the skin above the Trigeminal nerve auriculotemporal branch and the nodose ganglion and the caudal electrode at the skin above the carotid artery. Once attached, the PET backing was peeled off (Fig. 1a). The ZIF connector was attached to a breakout board (Adafruit Industries, Inc. NY, USA), which was then connected via cables to a biopotential data acquisition HackEEG board (Starcat LLC Seattle, WA) along with ground and reference electrodes (3 M Red Dot, 3 M, Inc—Saint Paul, MN). The impedance between the electrodes and the skin was measured by the Digitimer D360 amplifier (Digitimer Ltd, UK). Electrocardiography (ECG) was also monitored by the 3 M electrodes that were placed on the right upper chest and left bottom rib.

Data collection. Subjects were recruited at the University of California San Diego. Before the device application, the electrode placement area was abraded with abrasive pads (BIOPAC System Inc, Goleta, CA, USA) and prepped using alcohol pads to exfoliate the skin. A ground electrode was placed on the left forearm of the subject, and an additional reference cup electrode was placed ipsilaterally above the flexible sensor array at the mastoid. Data was collected and streamed to the open source HackEEG data acquisition system (Starcat LLC, Seattle WA, USA). The HackEEG is a high-performance, open-source Arduino Due shield for the Texas Instrument ADS1299 system on a chip. It can digitize 8-channel bio signals simultaneously at 24-bit analog–digital conversion resolution at 8000 samples per second with user-selectable gain from 1 to 24. The HackEEG system is enclosed in a 3D printed box with the dimensions of 13 cm × 7 cm × 5 cm (Fig. 1b).

Timed respiratory challenge. Respiration vital sign change was measured by a respiration belt transducer (BIOPAC system Inc, Goleta, CA, USA). The respiration belt was modified to function as a potentiometer, soldered in series with a 5 k ohm resistor that was powered by the 3.3 V power pin on the Arduino board. The voltage variation caused by the resistance change during each breath was measured by the HackEEG system as one of the biopotential channels. The respiration signal was filtered by a 5 Hz zero-phase low-pass filter in post-processing.

120 s after baseline recording, the subjects underwent a timed deep respiratory challenge. The timed respiratory challenge consisted of regular breathing (5 s inhale and 5 s exhale) that was carried out for 10 cycles. Post timed respiratory challenge data was then recorded for an additional 120 s. One subject's respiratory data was excluded due to irrevocable data loss.

Cold pressor test. Five minutes after the timed respiratory challenge, subjects were asked to perform the CPT task. Subjects were required to fully immerse their right hand into an ice water container to determine the cold pressor tolerance. Chilled water and freezer fresh ice (3 °C) were immediately added to the container with water temperature kept at 4–7 °C. Cold pressor tolerance was carried out for each subject; subjects were asked to keep their right hand in the ice water container for at least 1 min (5 min maximum) and only withdraw their hand if they could no longer tolerate the pain. Our surface electrodes have contact with the SCM and may detect EMG signals. Based on prior literature, we took precautions to minimize SCM activity[89,90]. Participants were instructed and monitored to avoid swallowing and talking, while subjects remained reclined (with pillow support) in an adjustable reclining chair; this position is known significantly reduce SCM EMG activity when compared to: (1) supine with head supported and (2) lateral decubitus with head supported, while standing also results in minimal SCM activity[89,90]. We also removed SCM EMG artifacts due to limb movement into and out of the ice bucket from all analysis.

Defined cold pressor test decreaser (CPTd) and cold pressor test increaser (CPTi). In this work, two common groups were identified: Cold Pressor Test increasers (CPTi) and Cold Pressor Test decreasers (CPTd). As previously defined by Mourot et al.[35], individuals in the CPTi group experienced increased HR when reacting to CPT, i.e., first an increase in HR was observed and then either a further increase in HR occurred, or the HR remained elevated until the end of the test. It should be noted that if HR decreased less than 5 beats, the HR was considered maintained, and the participant was categorized to the CPTi group. As previously defined by Mourot et al.[35], CPTd individuals were observed to react to the test with an initial increase followed by a decrease in HR of more than 5 beats per min (mean over 10 s) compared to the peak HR achieved during the test.

Data processing. A customized graphic user interface (GUI) installed on a Linux terminal was written in Python to monitor and display physiological signals in real time. In post processing, the cervical signal was filtered by a 20–1000 Hz zero-phase bandpass filter. Powerline noise and harmonics were also removed by notch filters. In each cervical neural recording, a spike sorting algorithm was carried out to differentiate detected spikes into different clusters. First, spike detection method adapted from works by Quiroga et al. was performed by setting a threshold as:

$$\text{Thr} = 3\sigma, \text{with}\, \sigma = median\left(\frac{|x|}{0.6745}\right)$$

where x is the bandpass filtered signal[91–93]. For each detected spike, a waveform of 80 samples (10 ms) was saved as the candidate waveform template, then aligned to their maximum at data point 30 (3.75 ms). Dimensionality reduction for feature extraction was run through T-distributed stochastic neighbor embedding (t-SNE) on all candidate spikes to enable a representative visualization[94]. The low dimensional projection was then run through density-based spatial clustering of application with noise (DBSCAN), an unsupervised classification algorithm[95], to cluster spikes into groups. The clustered neural groups were characterized by different firing rate and amplitude behaviors. The firing rate was counted as the number of neural group activity per second, and the amplitude was derived by calculating the peak-to-peak difference of each detected waveform (Fig. 1c).

Statistical analysis. Two-tailed paired sample t-test was used to identify differences between the firing frequency change of each individual channel when compared to baseline (Pre-CPT) activity across 5 intervals for the entire CPT duration (Fig. 4), as well as between each channel at each time interval (Fig. 4). The same methodology was used to test pairwise pre-to-post difference in (1) channel firing during the timed respiratory challenge (Fig. 5c), (2) HR change pre to post deep breathing challenge (Supplementary Fig. 1a), (3) channel

firing over the duration of the CPT challenge (Supplementary Fig. 1b), and (4) SCM EMG artifacts comparison for CPT (Supplementary Fig. 3a) for all within and between CPTd and CPTi group comparisons.

Two tailed two-sample t-test was used to compare neuronal firing differences between the CPTd (N = 5) and CPTi (N = 4) groups during the timed respiratory challenge, i.e., average firing frequency difference between the first and last 60 s of measurement (Fig. 5c) and SCM EMG artifacts comparison for deep breathing challenge (Supplementary Fig. 3b). All post-processing and statistical analysis were carried out with MATLAB software (MathWorks Inc, MA, USA).

To further understand interactions between groups (CPTi vs. CPTd) neural firing over time on each channel, spline generalized estimating equations (GEE)[96] across the whole time series and with knots at the 50 s and 200 s time points were used. The spline GEE models regressed firing frequency on time, group, and time by group interaction (Supplemental Fig. 2, Supplemental Table 1).

To further understand interactions between groups (CPTi vs. CPTd) neural firing during the timed respiratory challenge, a linear regression model with inference based on GEE was utilized. Differences in groups (CPTi vs. CPTd) neural firing pre-to-post the timed respiratory challenge were determined with the generalized estimating equations (Supplemental Table 2).

Data availability

Data is available at the authors' discretion upon direct request to the corresponding author.

Received: 23 June 2022; Accepted: 4 October 2022
Published online: 14 November 2022

References

1. McCorry, L. K. Physiology of the autonomic nervous system. *Am. J. Pharm. Educ.* **71**, 4 (2007).
2. Zygmunt, A. & Stanczyk, J. Methods of evaluation of autonomic nervous system function. *Arch. Med. Sci.* **6**, 11 (2010).
3. Marques, A. H., Silverman, M. N. & Sternberg, E. M. Evaluation of stress systems by applying noninvasive methodologies: Measurements of neuroimmune biomarkers in the sweat, heart rate variability and salivary cortisol. *NeuroImmun. Modul.* **17**, 205–208 (2010).
4. Jänig, W. & McLachlan, E. M. Characteristics of function-specific pathways in the sympathetic nervous system. *Trends Neurosci.* **15**, 475–481 (1992).
5. Levy, M. N., Koeppen, B. M. & Stanton, B. A. *Berne & Levy Principles of Physiology E-Book* (Elsevier Health Sciences, 2005).
6. Kaufmann, H., Norcliffe-Kaufmann, L. & Palma, J.-A. Baroreflex dysfunction. *N. Engl. J. Med.* **382**, 163–178 (2020).
7. Koopman, F. A. *et al.* Vagus nerve stimulation inhibits cytokine production and attenuates disease severity in rheumatoid arthritis. *Proc. Natl. Acad. Sci.* **113**, 8284–8289 (2016).
8. Hartmann, R., Schmidt, F. M., Sander, C. & Hegerl, U. Heart rate variability as indicator of clinical state in depression. *Front. Psych.* **9**, 735 (2019).
9. Bremner, J. D., Krystal, J. H., Southwick, S. M. & Charney, D. S. Noradrenergic mechanisms in stress and anxiety: I. Preclinical studies. *Synapse* **23**, 28–38 (1996).
10. Southwick, S. M. *et al.* Noradrenergic and serotonergic function in posttraumatic stress disorder. *Arch. Gen. Psychiatry* **54**, 749–758 (1997).
11. McFall, M. E., Murburg, M. M., Ko, G. N. & Veith, R. C. Autonomic responses to stress in Vietnam combat veterans with posttraumatic stress disorder. *Biol. Psychiat.* **27**, 1165–1175 (1990).
12. Southwick, S. M. *et al.* Abnormal noradrenergic function in posttraumatic stress disorder. *Arch. Gen. Psychiatry* **50**, 266–274 (1993).
13. Cramer, G. D. & Darby, S. A. *Clinical Anatomy of the Spine, Spinal Cord, and ANS* (Springer, 2017).
14. Thayer, J. F. & Sternberg, E. M. Neural aspects of immunomodulation: Focus on the vagus nerve. *Brain Behav. Immun.* **24**, 1223–1228 (2010).
15. Vonck, K. E. & Larsen, L. E. *Neuromodulation* 211–220 (Elsevier, 2018).
16. Lerman, I., Bu, T., Huang, M., Wu, V. & Coleman, T. Non-invasive targeted gastric vagal complex stimulation: Preliminary in human cutaneous measures of gastric slow wave function. *FASEB J.* **34**, 1–1 (2020).
17. Seki, A. *et al.* Sympathetic nerve fibers in human cervical and thoracic vagus nerves. *Heart Rhythm* **11**, 1411–1417 (2014).
18. Olshansky, B., Sabbah, H. N., Hauptman, P. J. & Colucci, W. S. Parasympathetic nervous system and heart failure: Pathophysiology and potential implications for therapy. *Circulation* **118**, 863–871 (2008).
19. Zanos, T. P. *et al.* Identification of cytokine-specific sensory neural signals by decoding murine vagus nerve activity. *Proc. Natl. Acad. Sci.* **115**, E4843–E4852 (2018).
20. Marmerstein, J. T., McCallum, G. A. & Durand, D. M. Direct measurement of vagal tone in rats does not show correlation to HRV. *Sci. Rep.* **11**, 1–12 (2021).
21. Sevcencu, C., Nielsen, T. N., Kjærgaard, B. & Struijk, J. J. A respiratory marker derived from left vagus nerve signals recorded with implantable cuff electrodes. *Neuromodulation* **21**, 269–275 (2018).
22. Metcalfe, B., Nielsen, T. & Taylor, J. in *2018 40th Annual International Conference of the IEEE Engineering in Medicine and Biology Society (EMBC)*. 1–4 (IEEE).
23. Ottaviani, M. M., Wright, L., Dawood, T. & Macefield, V. G. In vivo recordings from the human vagus nerve using ultrasound-guided microneurography. *J. Physiol.* **598**, 3569–3576 (2020).
24. Vallone, F. *et al.* Simultaneous decoding of cardiovascular and respiratory functional changes from pig intraneural vagus nerve signals. *J. Neural Eng.* **18**, 0460–0462 (2021).
25. Sevcencu, C., Nielsen, T. N. & Struijk, J. J. An intraneural electrode for bioelectronic medicines for treatment of hypertension. *Neuromodulation* **21**, 777–786 (2018).
26. Verma, N. *et al.* Microneurography as a minimally invasive method to assess target engagement during neuromodulation. *BioRxiv* **9**, 139 (2022).
27. Armour, J., Collier, K., Kember, G. & Ardell, J. Differential selectivity of cardiac neurons in separate intrathoracic autonomic ganglia. *Am. J. Physiol. Regul. Integrat. Comp. Physiol.* **274**, R939–R949 (1998).
28. Cassaglia, P. A., Griffiths, R. I. & Walker, A. M. Sympathetic nerve activity in the superior cervical ganglia increases in response to imposed increases in arterial pressure. *Am. J. Physiol. Regul. Integrat. Comp. Physiol.* **294**, R1255–R1261 (2008).
29. McLachlan, E. M., Davies, P. J., Häbler, H. J. & Jamieson, J. On-going and reflex synaptic events in rat superior cervical ganglion cells. *J. Physiol.* **501**, 165 (1997).
30. Seals, D. Sympathetic activation during the cold pressor test: influence of stimulus area. *Clin. Physiol.* **10**, 123–129 (1990).

31. Victor, R. G., Leimbach, W. N. Jr., Seals, D. R., Wallin, B. G. & Mark, A. L. Effects of the cold pressor test on muscle sympathetic nerve activity in humans. *Hypertension* **9**, 429–436 (1987).
32. Ghiasi, S., Greco, A., Barbieri, R., Scilingo, E. P. & Valenza, G. Assessing autonomic function from electrodermal activity and heart rate variability during cold-pressor test and emotional challenge. *Sci. Rep.* **10**, 1–13 (2020).
33. Hendriks-Balk, M. C. *et al.* Brainstem correlates of a cold pressor test measured by ultra-high field fMRI. *Front. Neurosci.* **14**, 39 (2020).
34. Elias, S. O. & Ajayi, R. E. Effect of sympathetic autonomic stress from the cold pressor test on left ventricular function in young healthy adults. *Physiol. Rep.* **7**, e13985 (2019).
35. Mourot, L., Bouhaddi, M. & Regnard, J. Effects of the cold pressor test on cardiac autonomic control in normal subjects. *Physiol. Res.* **58**, 83–91 (2009).
36. Limberg, J. K., Morgan, B. J., Schrage, W. G. & Dempsey, J. A. Respiratory influences on muscle sympathetic nerve activity and vascular conductance in the steady state. *Am. J. Physiol. Heart Circul. Physiol.* **304**, H1615–H1623 (2013).
37. Wang, S. *et al.* Mechanics of epidermal electronics. *J. Appl. Mech.* **79**, 3 (2012).
38. Dumitru, D., Amato, A. A. & Zwarts, M. J. *Electrodiagnostic Medicine* (Hanley & Belfus, 2002).
39. Kappenman, E. S. & Luck, S. J. The effects of electrode impedance on data quality and statistical significance in ERP recordings. *Psychophysiology* **47**, 888–904 (2010).
40. Huigen, E., Peper, A. & Grimbergen, C. Investigation into the origin of the noise of surface electrodes. *Med. Biol. Eng. Comput.* **40**, 332–338 (2002).
41. Rhudy, J. L., Williams, A. E., McCabe, K. M., Nguyên, M. A. T. V. & Rambo, P. Affective modulation of nociception at spinal and supraspinal levels. *Psychophysiology* **42**, 579–587 (2005).
42. Mischkowski, D., Palacios-Barrios, E. E., Banker, L., Dildine, T. C. & Atlas, L. Y. Pain or nociception? Subjective experience mediates the effects of acute noxious heat on autonomic responses. *Pain* **159**, 699 (2018).
43. Kim, D.-H. *et al.* Epidermal electronics. *Science* **333**, 838–843 (2011).
44. Kurniawan, J. F. *et al.* Electrochemical performance study of Ag/AgCl and Au flexible electrodes for unobtrusive monitoring of human biopotentials. *Nano Select* **3**, 1277–1287 (2022).
45. Kurniawan, J. F. *et al.* An adhesive-integrated stretchable silver-silver chloride electrode array for unobtrusive monitoring of gastric neuromuscular activity. *Adv. Mater. Technol.* **6**, 2001229 (2021).
46. Albulbul, A. Evaluating major electrode types for idle biological signal measurements for modern medical technology. *Bioengineering* **3**, 20 (2016).
47. Tallgren, P., Vanhatalo, S., Kaila, K. & Voipio, J. Evaluation of commercially available electrodes and gels for recording of slow EEG potentials. *Clin. Neurophysiol.* **116**, 799–806 (2005).
48. Kim, Y. S. *et al.* All-in-one, wireless, stretchable hybrid electronics for smart, connected, and ambulatory physiological monitoring. *Adv. Sci.* **6**, 1900939 (2019).
49. Kusayama, T. *et al.* Simultaneous noninvasive recording of electrocardiogram and skin sympathetic nerve activity (neuECG). *Nat. Protoc.* **15**, 1853–1877 (2020).
50. Subramanian, S., Purdon, P. L., Barbieri, R. & Brown, E. N. A model-based framework for assessing the physiologic structure of electrodermal activity. *IEEE Trans. Biomed. Eng.* **68**, 2833–2845 (2021).
51. Golding, J. & Stott, J. Comparison of the effects of a selective muscarinic receptor antagonist and hyoscine (scopolamine) on motion sickness, skin conductance and heart rate. *Br. J. Clin. Pharmacol.* **43**, 633–637 (1997).
52. MazloumiGavgani, A., Hodgson, D. M. & Nalivaiko, E. Effects of visual flow direction on signs and symptoms of cybersickness. *PLoS ONE* **12**, e0182790 (2017).
53. Gavgani, A. M., Nesbitt, K. V., Blackmore, K. L. & Nalivaiko, E. Profiling subjective symptoms and autonomic changes associated with cybersickness. *Auton. Neurosci.* **203**, 41–50 (2017).
54. Babic, T. & Browning, K. N. The role of vagal neurocircuits in the regulation of nausea and vomiting. *Eur. J. Pharmacol.* **722**, 38–47 (2014).
55. Zhong, W. *et al.* Mechanisms of nausea and vomiting: Current knowledge and recent advances in intracellular emetic signaling systems. *Int. J. Mol. Sci.* **22**, 5797 (2021).
56. Chen, M.-M., Xu, L.-H., Chang, L., Yin, P. & Jiang, Z.-L. Reduction of motion sickness through targeting histamine N-methyltransferase in the dorsal vagal complex of the brain. *J. Pharmacol. Exp. Ther.* **364**, 367–376 (2018).
57. Garcia-Agundez, A., Reuter, C., Caserman, P., Konrad, R. & Göbel, S. Identifying cybersickness through heart rate variability alterations. *Int. J. Virt. Real.* **19**, 1–10 (2019).
58. LaCount, L. T. *et al.* in *2009 36th Annual Computers in Cardiology Conference (CinC)*. 49–52 (IEEE).
59. Zhang, L. L. *et al.* Motion sickness: Current knowledge and recent advance. *CNS Neurosci. Ther.* **22**, 15–24 (2016).
60. Setiowati, N., Wijayanto, T. & Trapsilawati, F. in *IOP Conference Series: Materials Science and Engineering*. 012069 (IOP Publishing).
61. Task Force of the European Society of Cardiology the North America Electrophysiology. Heart rate variability: Standards of measurement, physiological interpretation, and clinical use. *Circulation* **93**, 1043–1065 (1996).
62. Lahiri, M. K., Kannankeril, P. J. & Goldberger, J. J. Assessment of autonomic function in cardiovascular disease: Physiological basis and prognostic implications. *J. Am. Coll. Cardiol.* **51**, 1725–1733 (2008).
63. Berntson, G. G. *et al.* Heart rate variability: Origins, methods, and interpretive caveats. *Psychophysiology* **34**, 623–648 (1997).
64. Kuo, T. B., Lai, C. J., Huang, Y. T. & Yang, C. C. Regression analysis between heart rate variability and baroreflex-related vagus nerve activity in rats. *J. Cardiovasc. Electrophysiol.* **16**, 864–869 (2005).
65. Murakami, H. *et al.* Evaluation of electrical activity after vagus nerve-preserving distal gastrectomy using multichannel electrogastrography. *J. Smooth Muscle Res.* **49**, 1–14 (2013).
66. Wisti, A. Z., D'Zmura, M. & Dennison, M. S. *Use of Physiological Signals to Predict Cybersickness* (Springer, 2022).
67. Dennison, M. S., Wisti, A. Z. & D'Zmura, M. Use of physiological signals to predict cybersickness. *Displays* **44**, 42–52 (2016).
68. Tan, Z. T. *et al.* Stomach region stimulated determines effects on duodenal motility in rats. *Am. J. Physiol. Regul. Integrat. Comp. Physiol.* **320**, R331–R341 (2021).
69. Lerman, I. *et al.* Noninvasive vagus nerve stimulation alters neural response and physiological autonomic tone to noxious thermal challenge. *PLoS ONE* **14**, e0201212 (2019).
70. Sclocco, R. *et al.* Neuroimaging brainstem circuitry supporting cardiovagal response to pain: A combined heart rate variability/ultrahigh-field (7 T) functional magnetic resonance imaging study. *Philos. Trans. R. Soc. A* **374**, 20150189 (2016).
71. Richter, C. G., Babo-Rebelo, M., Schwartz, D. & Tallon-Baudry, C. Phase-amplitude coupling at the organism level: The amplitude of spontaneous alpha rhythm fluctuations varies with the phase of the infra-slow gastric basal rhythm. *Neuroimage* **146**, 951–958 (2017).
72. Garland, E. L. Pain processing in the human nervous system: A selective review of nociceptive and biobehavioral pathways. *Prim. Care* **39**, 561–571 (2012).
73. Weise, F. *et al.* Effects of the cold pressor test on short-term fluctuations of finger arterial blood pressure and heart rate in normal subjects. *Clin. Auton. Res.* **3**, 303–310 (1993).
74. Shibahara, N. *et al.* The responses of skin blood flow, mean arterial pressure and RR interval induced by cold stimulation with cold wind and ice water. *J. Auton. Nerv. Syst.* **61**, 109–115 (1996).
75. Frey, M. & Selm, E. Reflex cardiovascular responses to cold exposure of the face or foot. *Jpn. Heart J.* **21**, 665–679 (1980).

76. Cui, J., Wilson, T. E. & Crandall, C. G. Baroreflex modulation of muscle sympathetic nerve activity during cold pressor test in humans. *Am. J. Physiol. Heart Circul. Physiol.* **282**, H1717–H1723 (2002).
77. Stancak, A., Yamamotova, A., Kulis, I. P. & Sekyra, I. V. Cardiovascular adjustments and pain during repeated cold pressor test. *Clin. Auton. Res.* **6**, 83–89 (1996).
78. Donaldson, G. W. *et al.* Pain and the defense response: Structural equation modeling reveals a coordinated psychophysiological response to increasing painful stimulation. *Pain* **102**, 97–108 (2003).
79. Minassian, A. *et al.* Association of predeployment heart rate variability with risk of postdeployment posttraumatic stress disorder in active-duty marines. *JAMA Psychiat.* **72**, 979–986 (2015).
80. Fu, Q. Autonomic dysfunction and cardiovascular risk in post-traumatic stress disorder. *Auton. Neurosci.* **237**, 102923 (2022).
81. Yoo, J.-K. *et al.* Abnormal sympathetic neural recruitment patterns and hemodynamic responses to cold pressor test in women with posttraumatic stress disorder. *Am. J. Physiol. Heart Circul. Physiol.* **318**, H1198–H1207 (2020).
82. Bu, Y. *et al.* in *North American Neuromodulation Society Meeting* (2022).
83. Bu, Y. *et al. Military Health System Research Symposium (MHSRS)* (Journal of MIlitary Trauma, 2021).
84. Debnath, S. *et al.* A method to quantify autonomic nervous system function in healthy, able-bodied individuals. *Bioelectron. Med.* **7**, 1–17 (2021).
85. Huang, M. *et al.* Early sympathetic neural responses during a cold pressor test linked to pain perception. *Clin. Auton. Res.* **31**, 215–224 (2021).
86. Nepomuceno, V., Nepomuceno, E., Regalo, S., Cerqueira, E. & Souza, R. Electromyographic study on the sternocleidomastoid and pectoralis major muscles during respiratory activity in humans. *J. Morphol. Sci.* **31**, 098–102 (2014).
87. Estrada, L. *et al.* in *Libro de Actas del XXXIII Congreso Anual de la Sociedad Española de Ingeniería Biomédica*, 183–186.
88. Clark, F. & von Euler, C. V. On the regulation of depth and rate of breathing. *J. Physiol.* **222**, 267–295 (1972).
89. Palazzi, C. *et al.* Body position effects on EMG activity of sternocleidomastoid and masseter muscles in patients with myogenic cranio-cervical-mandibular dysfunction. *Cranio* **14**, 200–209 (1996).
90. De Mayo, T. *et al.* Breathing type and body position effects on sternocleidomastoid and suprahyoid EMG activity. *J. Oral Rehabil.* **32**, 487–494 (2005).
91. Quiroga, R. Q., Nadasdy, Z. & Ben-Shaul, Y. Unsupervised spike detection and sorting with wavelets and superparamagnetic clustering. *Neural Comput.* **16**, 1661–1687 (2004).
92. Rey, H. G., Pedreira, C. & Quiroga, R. Q. Past, present and future of spike sorting techniques. *Brain Res. Bull.* **119**, 106–117 (2015).
93. Navajas, J. *et al.* Minimum requirements for accurate and efficient real-time on-chip spike sorting. *J. Neurosci. Methods* **230**, 51–64 (2014).
94. Van Der Maaten, L. Accelerating t-SNE using tree-based algorithms. *J. Mach. Learn. Res.* **15**, 3221–3245 (2014).
95. Ester, M., Kriegel, H.-P., Sander, J. & Xu, X. in *Kdd*, 226–231.
96. Tang, C. Y. & Qin, Y. An efficient empirical likelihood approach for estimating equations with missing data. *Biometrika* **99**, 1001–1007 (2012).

Acknowledgements

The authors would also like to acknowledge Marcelo Aguilar and Jamie Burks for their useful discussion.

Author contributions

I.L., T.C. proposed the experimental concept. I.L., T.C., Y.B. and J.K. designed methodology and experiments. R.R. suggested experimental improvements. J.K., A.N., N.S., T.P., V.W., B.T., A.S. designed the surface electrode. B.H. designed graphic user interface. Y.B., J.K., A.N. collected data. Y.B. analyzed data. T.W., X.T. suggested statical plan and conducted statistical analysis. I.L., Y.B. and J.P. wrote the primary content of the paper. All other authors participated in the editing of the final manuscript.

Funding

Funding was provided by Biomedical Advanced Research and Development Authority (Grant No. 75A50119C00038), Further funding was provided by the David and Janice Katz Neural Sensor Research Fund in Memory of Allen E. Wolf.

Competing interests

The authors declare no competing interests.

Additional information

Supplementary Information The online version contains supplementary material available at https://doi.org/10.1038/s41598-022-21817-w.

Correspondence and requests for materials should be addressed to Y.B.

Reprints and permissions information is available at www.nature.com/reprints.

Publisher's note Springer Nature remains neutral with regard to jurisdictional claims in published maps and institutional affiliations.